Journal of
Materials Chemistry C

ROYAL SOCIETY
OF CHEMISTRY

COMMUNICATION

View Article Online
View Journal | View Issue

Cite this: *J. Mater. Chem. C*, 2025, **13**, 20000

Received 29th July 2025,
Accepted 1st September 2025

DOI: 10.1039/d5tc02865e

rsc.li/materials-c

Wearable, near temperature insensitive laser-induced graphene nanocomposite strain sensors

Tom Jacquin,†[a] Simon Wanstall, †[bc] Inkyu Park, [d] Adam A. Stokes,[e]
Hadi Heidari, [a] Theodore Lim[bc] and Morteza Amjadi *[a]

Soft and flexible sensors offer a potential paradigm shift in wearable bioelectronics to enhance human–machine interfacing for diagnosis, healthcare monitoring, and prosthetic applications. Soft nanocomposite strain sensors have emerged as a promising solution for the real-time monitoring of biomedical signals due to their conformability, stretchability, and resilience to different strain levels. Nonetheless, these sensors are susceptible to external factors like temperature variations, impeding their functionality in real-world applications. This paper introduces a strategy to tackle the considerable temperature sensitivity of nanocomposite strain sensors by fine-tuning the electrothermal properties of laser-induced graphene nanocomposites. The controlled manipulation of laser parameters governs the carbonization process, and the formation of 3D interconnected conductive networks, leading to nanocomposite strain sensors with temperature sensitivities as low as 0.25% °C^{-1}. These sensors enable real-time strain sensing with minimal interference from thermally induced noise in environments prone to significant temperature fluctuations, such as haptic feedback in prosthetics when grasping hot and cold drinks. Additionally, integrating this approach into the design of electrothermal soft actuators results in a self-sensing soft actuator with near-zero temperature sensitivity up to 100 °C, further demonstrating the versatility of these nanocomposite sensors.

1 Introduction

In recent years, biomedical studies have emerged as a particularly data-intensive domain, prompting substantial research and development efforts to meet the escalating data-gathering requirements. The demand for more patient-centered data is not simply desirable, but a need, to advance better healthcare and well-being.[1,2] Consequently, there has been a remarkable surge in the exploration of novel sensing devices tailored for biomedical applications. Real-time prolonged monitoring of biomedical signals benefits from using soft wearable sensors capable of accommodating the irregular surfaces of the skin while enduring both small and large strains, such as those encountered during blood pressure measurements or limb movement.[3–5] Soft sensors have gained prominence as they offer a range of advantages over rigid sensors, including enhanced biocompatibility, reduced cytotoxicity, and overall comfort.[6,7] As a result, soft sensors are gradually replacing their rigid counterparts in medical devices and prosthetics.[8,9]

Among various wearable sensors, soft resistive-type strain sensors typically consist of functional composite structures comprising a soft supporting material, such as silicone-based polymers (*e.g.*, polydimethylsiloxane (PDMS) and Ecoflex), and a strain sensing film made of materials including metal nanowires,[10–14] nanomeshes,[15] liquid metals,[16] carbon nanotubes,[17–19] and conductive polymers.[20,21] These micro/nano-scale materials form a percolation network that enables electronic transport through intrinsic mechanisms and contact points between adjacent nanomaterials, or *via* quantum tunnelling effects when they are separated by a thin polymer matrix.[22] In strain sensors, this percolation network is primarily sensitive to stretching and exhibits sensitivity to various other undesired stimuli as well. When these sensors are subjected to mechanical strain, the increased distance between materials results in an elevated electrical resistance.

To enhance the performance of soft strain sensors, researchers have explored diverse strategies, including the introduction of microcracks to improve sensitivity,[5,23–26] the utilization of optimized sensing elements, and doping of the sensing element.[27–29] Li *et al.* studied a 3D crack conductive network strategy based on spray-coated PDMS to overcome low fidelity and high hysteresis of soft strain sensors.[30] Amjadi *et al.*

---

[a] *James Watt School of Engineering, University of Glasgow, G12 8QQ, UK. E-mail: Morteza.Amjadi@glasgow.ac.uk*
[b] *Edinburgh Centre for Robotics, Heriot-Watt University, Edinburgh, EH14 4AS, UK*
[c] *School of Engineering and Physical Sciences, Heriot-Watt University, Edinburgh, EH14 4AS, UK*
[d] *Department of Mechanical Engineering, Korea Advanced Institute of Science and Technology (KAIST), Daejeon, Republic of Korea*
[e] *Institute of Integrated Micro and Nano Systems, School of Engineering, University of Edinburgh, EH9 3FF, UK*

† Tom Jacquin and Simon Wanstall contributed equally to this work.

introduced a highly stretchable and sensitive strain sensor based on a silver nanowires–elastomer nanocomposite, addressing the challenges of hysteresis and enhancing sensor performance.[11] Wu *et al.* proposed a double-layer network formed of graphene foam and poly(3,4-ethylenedioxythiophene) polystyrene sulfonate (PEDOT:PSS) to manufacture temperature-insensitive strain sensors utilizing the electrothermal properties of both graphene and PEDOT:PSS.[31] Moreover, previous works by Amjadi *et al.* have achieved tunable strain sensor sensitivity and high signal-to-noise ratio (SNR) self-sensing soft actuators using simple hybrid carbon-based nanocomposites.[32,33] Further applicable research in the wider soft wearable electronics field has explored improving robustness and sensor performance through laser sintering or ablation of composite materials,[34–36] as well as overcoming material weaknesses (*e.g.*, oxidization of metal nanowires) through air-tight encapsulation.[37]

One particular sensing material has received significant attention in recent years—laser-induced graphene (LIG). First discovered in 2014 by Lin *et al.*, LIG was first generated by irradiating polyimide (PI) films with a proprietary laser engraver.[38] The off-the-shelf components and widely available laser technology offer a rapid and cost-effective method for producing thin layers of disordered, porous graphene in virtually any 2D shape.[39] Controlled laser parameters dictate carbonization and the formation of interconnected graphene networks, while gas released during the process creates pores and voids within the microstructure.[40] This dual mechanism results in a porous 3D architecture.[41,42] LIG provides a faster, cheaper and overall, more accessible manufacturing process than graphene produced through other methods, such as chemical vapor deposition.[43–45] The versatility of LIG-based sensors has been demonstrated through successful applications in strain,[46–48] pressure,[49,50] and chemical sensing.[51–53] The study has since been expanded to encompass a broader array of precursor materials for LIG formation. Diverse materials such as Kevlar, polysulfones, poly(ether imide), polyphenylene sulphide, and lignin have been directly converted to LIG. Polysaccharides like cellulose and starch have also been effectively activated for conversion into LIG through the application of boric acid or phosphate-based fire retardants as well as conversion under controlled gas atmospheres.[54–58] This versatility has led to the creation of inexpensive biodegradable electronics, bringing more research attention to LIG for a more sustainable future.[59,60] The porosity of LIG means it can be transferred to more stretchable substrates (*e.g.*, PDMS) to enhance its flexibility and stretchability, enabling its use in diverse wearable and skin-interfacing applications.[61,62] The compatibility of LIG with polymer precursors and encapsulants can be further leveraged to generate conductive 3D structures *via* PI powder-based additive manufacturing.[63] Despite the numerous advantages of LIG nanocomposite soft strain sensors, they are not without limitations. For instance, the electrical resistance of graphene decreases with increased temperature, elastomers expand when heated, and the porous structure of LIG allows humidity to affect its electrical conductivity.[64] These effects can potentially interfere with their sensing functions. However, if these drawbacks could be minimized, the unique accessibility of LIG could spark accelerated progress in the field of soft wearable sensors.

Researchers have successfully made strides to overcome some of the limitations of the LIG sensors. For instance, Huang *et al.* achieved low hysteresis and high durability by creating a LIG-silicone rubber strain sensor with a wavy structure.[65] In another example of structural improvements, W. Wang *et al.*, inspired by the shape of the human fingerprint, developed a LIG-Ecoflex strain sensor with enhanced sensitivity due to microcracks in the conductor.[66] A multi-functional, wearable e-skin has been created by H. Wang *et al.* with serpentine LIG temperature sensors that are insensitive to strain alongside strain sensors so that their temperature sensitivity can be counteracted.[67] Though effective, this technique relies on an extra computation step to compensate for the temperature sensitivity of the LIG strain sensors. There are many applications where computation and power are limited resources, so this sensor-based temperature compensation technique would not be ideal. Despite the previously discussed advancements, it remains challenging to fabricate soft and stretchable strain sensors with durable sensing performance under transient environmental conditions through a facile and scalable manufacturing process.

Herein, we present a strategy for reducing the temperature sensitivity of LIG–PDMS nanocomposite sensors by tuning the laser parameters during production. This exploits the counteractive relationship between the negative temperature coefficient of resistance (TCR) of LIG and the positive coefficient of thermal expansion (CTE) of PDMS. Our analysis shows that tuning the laser induction process can adapt the physical microstructure of the nanocomposite to be less sensitive to temperature changes. Our approach results in conductive nanocomposite strain sensors with temperature sensitivities as low as 0.25% $^{\circ}C^{-1}$ and self-sensing PI-LIG–PDMS electrothermal actuators with near-zero thermal noise up to 100 °C. Furthermore, the gauge factors (GFs) of our LIG nanocomposite strain sensors range from 16 to 110. By diminishing the impact of temperature variations on soft nanocomposites, our research expands the capabilities of current soft wearable strain sensors for low-noise strain measurement within temperature-varying environments. Developing wearable and temperature self-compensating LIG nanocomposite sensors through low-cost, scalable digital manufacturing could prove advantageous for numerous fields, including biomedicine, soft robotics, and human–machine interfaces like prosthetics.

2 Results and discussion

The soft strain sensors were manufactured using the process schematically shown in Fig. 1(a) (see Experimental Section for more details). PI films with a thickness of 150 μm were attached to a flat glass plate and used as the starting material for producing the sensors. A commercial CO_2 laser engraver was used to convert the PI material into a 3D porous conductive

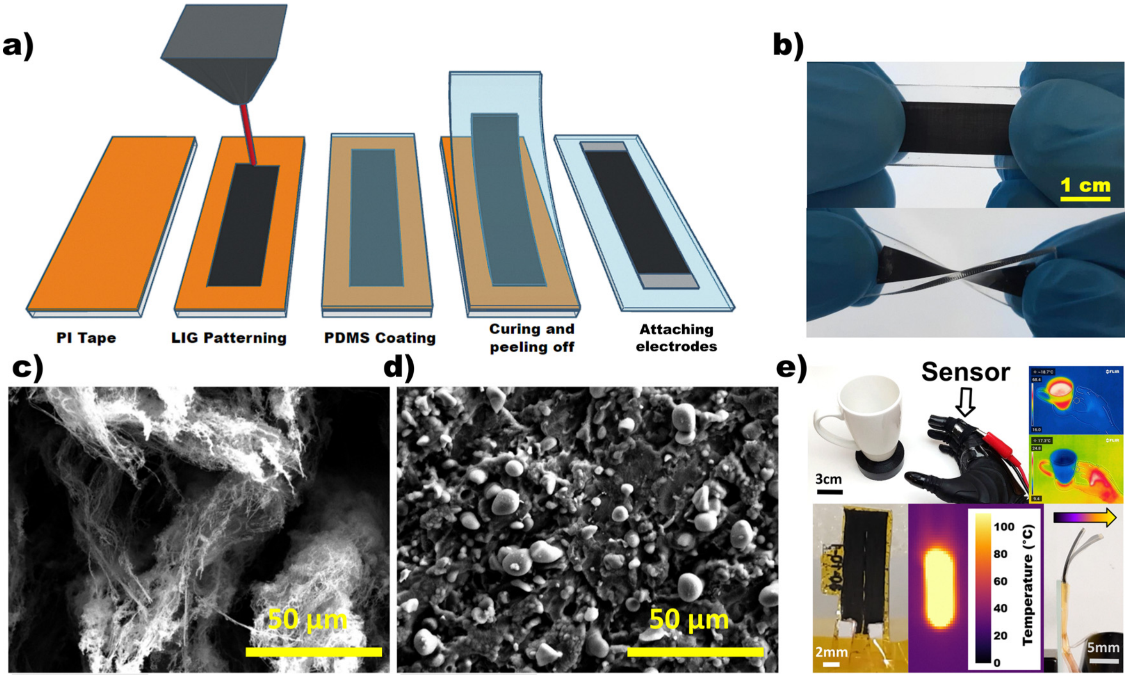

Fig. 1 (a) Manufacturing process of LIG–PDMS nanocomposite strain sensors. (b) Photographs of a LIG–PDMS strain sensor demonstrating its softness and stretchability. (c) SEM image of a native LIG sample before elastomer coating, showing the 3D porous structure of the LIG. (d) SEM image of the fabricated LIG–PDMS nanocomposite, revealing infiltration of the PDMS into the LIG network. (e) Application demonstrations of nanocomposite strain sensors including consistent grasping feedback for hot or cold objects and self-sensing heat-activated actuators.

graphene network. While various types of lasers can be employed for LIG fabrication, a CO_2 laser was selected due to its ability to produce high-quality LIG with comparatively larger pore sizes.[68,69] To fabricate LIG–PDMS nanocomposite sensors, a 10 : 1 mixture of PDMS base and curing agent was prepared, degassed in a vacuum chamber, subsequently poured onto the PI-LIG surface, and degassed again to ensure its complete infiltration into the porous carbonized film. The coated elastomer film was cured at 100 °C for one hour to form a robust nanocomposite film of LIG and PDMS elastomer. The PDMS layer with embedded LIG film was then peeled off from the substrate and trimmed into rectangular-shaped sensor samples with high flexibility and stretchability, as shown in Fig. 1(b). Electrodes were attached to both sides of each sample using conductive silver epoxy for electrical measurements. For comparison, LIG samples without elastomer coating were also manufactured by directly applying electrodes to the raw LIG films.

The microstructure of the LIG nanocomposite was observed by taking scanning electron microscope (SEM) images of samples before and after elastomer coating. Fig. 1(c) highlights the formation of the LIG during the lasing process. The intense, localized heat generated by the laser rapidly decomposes the precursor material, leading to the liberation of gases such as carbon dioxide, carbon monoxide, and hydrogen.[45] These gases create high-pressure conditions that promote the reorganization of carbon atoms into the hexagonal lattice characteristic of graphene. Simultaneously, this gas release creates 3D porous microstructures as can be seen in the SEM image. This highly porous structure enables the liquid PDMS elastomer to penetrate the conductive network and fill all voids. When the liquid elastomer is fully cured, the infiltration process results in highly robust, stretchable, and conductive nanocomposite films (Fig. 1(b)). Fig. 1(d) shows the SEM image of the LIG–PDMS nanocomposite structure, revealing that all gaps present in the native porous LIG are filled by the elastomer. The LIG–PDMS nanocomposites have applications in many areas of the biomedical field, and we chose to showcase this with prosthetic haptic strain sensors that are consistent whether grasping hot or cold beverages, and temperature-invariant, self-sensing, thermally activated soft actuators (Fig. 1(e)).

To examine the influence of the lasing parameters on electromechanical and electrothermal properties of the LIG nanocomposites, we manufactured different samples by varying the lasing power and speed (Fig. S1). Hereafter, we represent each sensor sample in all figures by %power_%speed notation, displaying which settings were used with our laser engraver to produce it. Hence, LIG sample 20_7 is made using 20% laser power and 7% processing speed, or 12 W at 0.196 m s^{-1} (full conversions are available in Table S1).

As part of a comprehensive analysis, we initially investigated the *I*–*V* characteristics of both pure LIG and a LIG–PDMS nanocomposite by varying the applied voltage across each sample while measuring the electrical current. The results in Fig. S2 reveal that both samples possess linear ohmic properties within the tested voltage range. Moreover, native LIG on PI exhibits a negative TCR, which indicates that its resistance decreases as the temperature increases (see Fig. S3a and b). This electrothermal behavior is primarily attributed to the

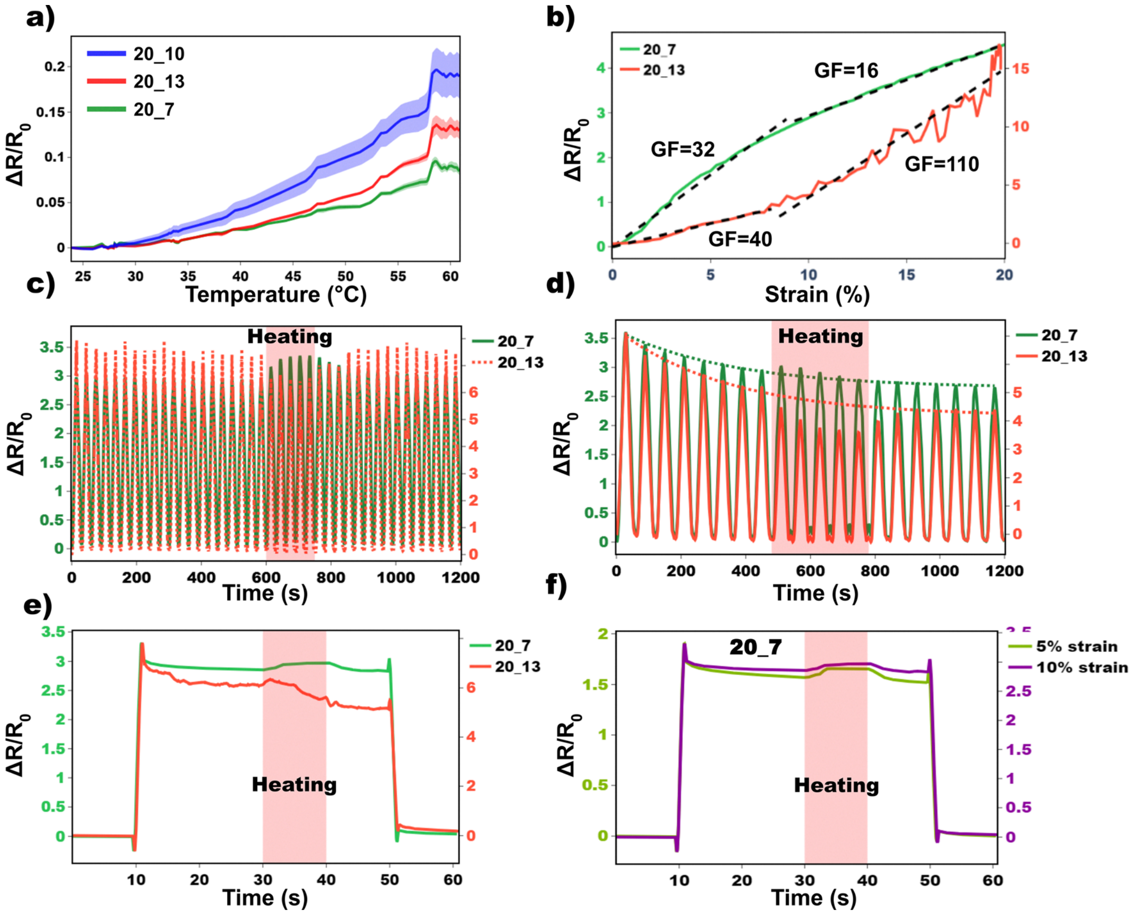

Fig. 2 (a) Static electrothermal response of LIG–PDMS composites for different lasering speeds at 20% power. (b) Strain resistance curve for two sets of sensors produced at 20% power, comparing 7% and 13% speeds. (c) Effect of heating on samples during cyclic stretching (10% strain applied) at a high strain rate. (d) Effect of heating on strain testing at a slower strain rate (10% strain applied). (e) Effect of heating on samples during static loading (10% strain applied). (f) Effect of strain on thermal sensitivity of a 20_7 strain sensor. The sensor was held at 5 and 10% strain while an identical thermal load was applied for each strain level.

increase in carrier mobility and thermal excitation of charge carriers, resulting in enhanced electrical conductivity at higher temperatures.[70] Our experimental data show that the electrothermal properties of uncoated LIG are minimally affected by laser parameters (*i.e.*, power and scanning speed). For all tested speeds and powers, a decrease of approximately 2–2.5% in resistance was measured at 60 °C (see Fig. S3a and b).

In contrast to the native LIG, the LIG–PDMS nanocomposites demonstrate significant variations in the electrothermal response depending on the laser settings employed (see Fig. 2(a) and Fig. S3c, d). For instance, when the temperature was increased from room temperature ($\sim$18 °C) to 60 °C, a 20% increase in resistance was observed for a 20_10 nanocomposite sample, compared to a 7% increase for a 20_7 sample. The LIG–PDMS nanocomposite incorporates a PDMS elastomer matrix that possesses a CTE of around 310×10^{-6} $^\circ\mathrm{C}^{-1}$.[71] Consequently, the thermal expansion of the PDMS matrix leads to alterations in the interparticle spacing and contact resistance between the graphene particles within the LIG percolation network. As the temperature increases, the expansion of the PDMS matrix causes a reduction in contact density and the efficiency of charge transport pathways between the graphene particles, resulting in an increase in the resistance of the nanocomposite. Furthermore, penetration of the liquid PDMS into the 3D porous microstructure of LIG creates tunnelling junctions among several graphene particles which are not physically connected but distanced closely. Variations in the temperature of the nanocomposite influence the tunnelling current within the network. Thermal expansion of PDMS and formation of the tunnelling junctions together with the intrinsic negative TCR of the LIG contribute to the overall electrothermal properties of the nanocomposite.[11,22] Although the increase in resistance of all LIG–PDMS samples can be attributed to the positive CTE of PDMS, the underlying mechanism remains unclear. The nanocomposite samples exhibit varying thermal responses, yet the relationship between laser fluence (*i.e.*, laser energy delivered per unit area) and thermal sensitivity is nonlinear, and the thermoresistive behavior of native LIG shows minimal dependence on laser fluence.

We further investigated the observed thermoresistive effects and explored whether changing the lasing parameters could decouple thermal and mechanical sensing in the LIG–PDMS nanocomposite stretchable strain sensors. Although the concept of flexible temperature-invariant strain sensors has been studied,[31] our approach provides a rapid, digital, and scalable manufacturing process, using inexpensive (∼£1 per sensor), off-the-shelf materials, for developing wearable strain sensors with controllable electrothermal behaviour. Fig. 2(b) depicts the electromechanical response of two nanocomposite strain sensor samples subjected to 20% stretching. These were manufactured with the same lasing power of 20% but at different processing speeds. The curve illustrates the relationship between the applied strain and the corresponding change in resistance. As shown in the figure, each sample exhibits distinct changes in the electrical resistance during the stretching cycle. The sample processed at a lower laser speed exhibits significantly reduced hysteresis (1%) compared to 14% for the higher-speed sample (see Fig. S4 for details of the hysteresis calculation). Moreover, the sample produced with lower laser processing speed demonstrates diminished sensitivity, reflected in lower GF – relative changes in the resistance divided by the applied mechanical strain – ranging from 16 to 32. Strain sensors produced with this speed setting exhibited a distinctive concave strain/resistance curve, suggesting higher sensitivity at lower strains. In contrast, sensors generated at the higher speed portray convex strain/resistance curves, indicating a more pronounced sensitivity at higher strains, with GFs in excess of 110 (Fig. 2(b), Fig. S5 and Table S1). While soft sensors with higher GFs have been reported in the literature,[22] this aspect falls outside the scope of the current study. For instance, strategies such as incorporating cracks into the design of soft stretchable strain sensors have been shown to improve the GF.[72] Differences in strain response between our sensors arise from variations in the microstructure of the conductive network. Compared to higher fluence sensors, sensors induced with lower fluence feature a thinner, less interconnected layer of LIG, offering higher sensitivities due to their low-density conductive networks (Fig. S1). Despite their greater sensitivity, low fluence strain sensors exhibit higher measurement noise, as shown in Fig. 2(b). The electromechanical response of a 20_7 sensor was further evaluated under repeated loading–unloading cycles. As shown in Fig. S6, the sensor exhibited durable response over 1000 cycles, loading from 0 to 20% strain.

Additional tests were conducted to investigate the dynamic electrothermomechanical response of strain sensor samples manufactured with different lasing parameters. As illustrated in Fig. 2(c) and (d), both 20_7 and 20_13 sensors underwent cyclic mechanical stretching from 0 to 10% strain with periods of 30 and 60 s, respectively. The initial drift in the cyclic strain response of soft strain sensors is well-documented,[61,73] so the maxima at ambient conditions have been overlaid in Fig. 2(d) for clarity. While under dynamic mechanical loading, the sensors were subjected to an abrupt temperature shift from room temperature (∼18 °C) to 100 °C for 5 cycles. The cycle duration, whether 30 or 60 seconds, did not significantly alter the overall trend in resistance change when heated, indicating that the relaxation time of the PDMS did not alter the response to an increase in temperature. The 20_7 sensors showcased a positive change in resistance, reaching up to 3%. Conversely, the 20_13 nanocomposite sample exhibited a negative relative change in resistance, surpassing 15%. This experimental investigation reveals a pronounced trend: the TCR within LIG–PDMS nanocomposite sensors under dynamic mechanical loading exhibits variability based on specific laser settings used during fabrication. These dynamic TCR profiles can assume positive, negative, or nearly neutral values, contingent on manufacturing intricacies. As shown in Fig. 2(e), the sensors were further evaluated using a specific testing protocol wherein the samples were first subjected to a 10% static strain and held for 20 s. Afterwards, they were heated for 10 s, followed by a cooling period of 10 s before being unloaded. Despite the static nature of the test, sensors exhibited consistent responses to the previous dynamic tests.

The difference observed in dynamic TCR results from complex interactions, primarily driven by the interplay between the relaxation and expansion of PDMS within the nanocomposite structure when heated and the interconnectivity and TCR of the LIG network itself. When PDMS is heated, it undergoes faster stress relaxation, altering the strain distribution within the sample. This could explain the drop in the dynamic strain response of 20_13 sample when heated. Additionally, the limited positive response of 20_7 to heating is likely due to the opposing effects of the negative TCR of LIG and the positive CTE of PDMS. These conclusions are further supported by the relaxation of a pure PDMS film with identical dimensions to the sensors, when it was heated under tension, reducing the force needed to stretch it (Fig. S7). We also find that, as strain levels increase, the relative change in resistance due to temperature increase diminishes. For instance, the resistance increase is 4% at 10% strain, compared to 6% at 5% strain for a 20_7 strain sensor (Fig. 2(f)). This suggests a complex interplay between strain-induced and temperature-induced resistance changes in sensors. Therefore, operating the sensors at higher strains could help minimize the relative impact of temperature-induced resistance variations.

To study the physical phenomena behind the varying electrothermomechanical properties of LIG nanocomposite sensors, they were investigated with Raman spectroscopy. The acquired Raman spectra were analyzed to determine characteristic features such as the G band (graphitic sp^2 carbon), D band (disordered carbon), and 2D band (second-order overtone of the D band). The intensity ratio of the D and G bands (I_G/I_D) was calculated to assess the quality and structural characteristics of the LIG. Fig. 3(a) displays the representative Raman spectra of the raw LIG samples. The G band is observed at 1580 cm^{-1}, the D band at 1350 cm^{-1}, and the 2D band at 2700 cm^{-1}. The obtained Raman spectra confirm the successful conversion of the PI film into LIG. The presence of the characteristic G, D, and 2D bands in the spectrum indicates the formation of graphitic carbon with a certain degree of disorder. The calculated I_G/I_D ratio around 1 aligns with values reported in the literature and is indicative of a substantial degree of graphene formation within the LIG films (see Fig. S8).[38,74] Comparing our findings with previous studies,[38,74–76] the observed Raman features, and calculated parameters align with the reported

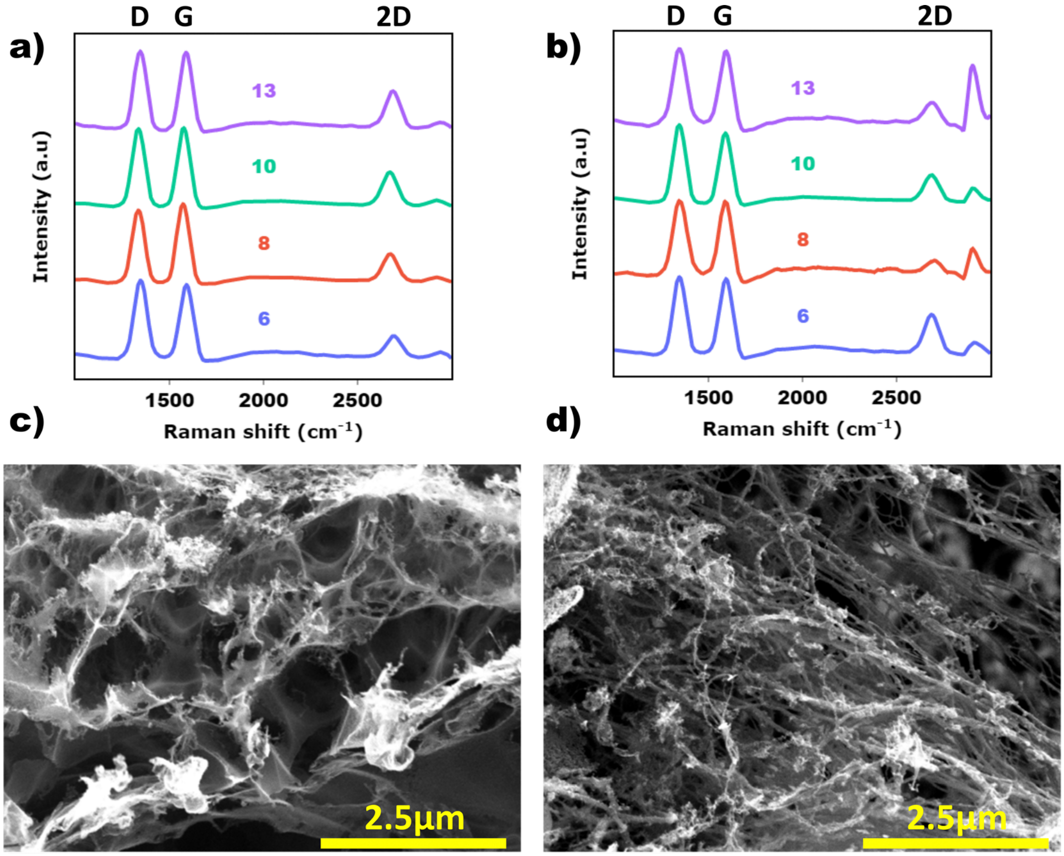

Fig. 3 (a) Raman spectrum and analysis for pure LIG samples made with 20% laser power and 13%, 10%, 8% and 6% processing speeds, from top to bottom. D, G and 2D peaks are labelled above. (b) Raman spectrum and analysis for the LIG–PDMS nanocomposites with the same lasing parameters as in (a). (c) SEM image of a 20_13 raw LIG sample. (d) SEM image of a 20_7 raw LIG sample.

characteristics of high-quality graphene materials. Fig. 3(b) underscores the resemblance in graphene structure between the raw samples and the LIG–PDMS nanocomposites, implying that the structural integrity and quality remain unaffected throughout the elastomer infiltration and transfer process. Additionally, the Raman analysis revealed no discernible differences between the spectra of high and low fluence samples, suggesting that any observed differences in the electrothermomechanical performance are not related to variations in graphene quality or atomic structure.

In-depth exploration of the graphene structure through SEM (Fig. 3(c) and (d)) analysis revealed a correlation: heightened fluence during fabrication results in a more porous graphene microstructure with a more intricately connected graphene network (Fig. S9). After the PDMS infiltration to form a nanocomposite material (see cross-sectional SEM images in Fig. S10), these varying LIG microstructures directly govern the strain sensing behavior, tunnelling junctions, and overall properties of the nanocomposite. For instance, 20_7 samples possess highly porous, thin, hierarchical fibrous structures, which can lead to greater numbers of tunnelling junctions within the network. When the strain sensor is heated, the high thermal expansion of the elastomer increases the tunnelling distance among the abundant, closely spaced particles, resulting in a slight increase in the electrical resistance, as evident in our experimental observation (Fig. 2(c) and (d)).[22] In the case of low fluence samples (*e.g.*, 20_13), the electrical conduction is mostly formed by thick, branching, conductive traces of the LIG. Even after elastomer penetration, there are still plenty of physically connected graphene particles. Consequently, the intrinsic negative TCR of the LIG significantly contributes to the response of the nanocomposite to elevated temperatures. Therefore, observed differences in sensor performance are likely due to variations in the LIG microstructure rather than the chemical composition. This analysis provides an explanation for the influence of laser fluence on the thermoresistive behavior of both native LIG and LIG–PDMS nanocomposites. The CTE of the PDMS has more influence than the negative TCR of graphene on LIG samples made with high enough laser fluences to be restructured into fibrous networks by the exhaust gases. The effect is further pronounced in dynamic tests when the sensors are stretched, and their percolation networks are dominated by different conductive pathways depending on their microstructures.

We have illustrated that the electrothermomechanical properties of the LIG–PDMS nanocomposite can be tuned by adjusting the lasing parameters, enabling the design of nearly heat-insensitive strain sensors through a scalable, low-cost, and accessible process. The results suggest that complete eradication of temperature sensitivity is likely possible for tuned LIG–PDMS nanocomposites. However, the chaotic nature of the laser induction process means that more research is needed to find a similarly facile and repeatable process to produce such a material. Previous studies using graphene–elastomer nanocomposites produced without laser induction have achieved near-zero TCRs by exploiting a similar mechanism (negative TCR *versus* positive CTE).[77,78] However, these solutions require more preparation, specialized equipment and more expensive precursor materials than our procedure, making them less facile. Niu *et al.*[78] made sensors (TCR $\sim 0.7 \times 10^{-4}\ \mathrm{K}^{-1}$) that could maintain near-zero TCR from − 40 °C up to room temperature, but their layered drop-coating process was slower and less precise than laser patterning and encapsulation. Our soft sensors have potential for use in a variety of applications, with a reduced need for calibration and compensation of the unwanted noise generated by transient changes in temperature. In the following, we highlight the use of our LIG nanocomposites in highly temperature-variant wearable and soft robotic applications where somatic sensing remains challenging. We selected sample 20_7 for the following applications, as it exhibited the best performance in terms of stability and response under varying thermal conditions, making it suitable for integration into environments with fluctuating temperatures.

Prosthetic soft strain sensor

This application of the LIG–PDMS nanocomposite strain sensors demonstrates the influence of thermally induced noise on a sensor that is optimized to have reduced sensitivity to temperature, in a real-life scenario. The scenario chosen involved tracking the motion of a robotic prosthetic hand while grasping a mug full of hot and cold water to simulate a prosthesis user picking up drinks. This experiment applies to the current state of the art in prosthetics research because users greatly benefit from haptic feedback from mechanisms like strain and pressure that give them more information about what their prosthesis is doing or touching.[79,80] The disruptive influence of temperature on the signal from the strain sensor, in this case, is significant because an inconsistent signal could be fed back to a user depending on whether they are holding a cold or dangerously hot beverage. This could then lead to the user dropping what they are holding and becoming injured by scalding liquids and/or smashed drink vessels.

Fig. 4(a) shows the Covvi™ robotic prosthetic hand with a 20_7 strain sensor wrapped around the index finger and secured with a kinesiology tape. As shown in Fig. 4(b), this configuration causes the sensor to bulge outwards when the finger bends into a grasp, generating a strain on the sensitive zone of the LIG strain sensor and inducing a measurable resistance change. The sensor device is a long strip, mainly consisting of PDMS so that it can be wrapped around the finger and secured with tape in such a way that this bulging occurs. An added benefit of this design is that the edges of the LIG area, where the electrodes are attached, experience little disturbance during grasping. Fig. 4(c) is a photograph of the application scenario, wherein the sensor on the hand is connected to a multimeter by wires secured to the wrist of the prosthetic, and a mug is positioned to be grasped by the hand while it contains hot or cold water. The mug was placed on a pedestal during the experiment to allow the hand to fit around a smaller diameter area for a more secure grip.

Fig. 4(d) illustrates the strain response of an optimized sensor during the exercises of grasping the mug when it contains hot (~70 °C) and cold (~8 °C) water (see Movie S1). Each activity involved three cycles of grasping the mug, holding for 40 s, releasing and waiting for 60 s. The purpose of the hold duration is to allow time for the temperature of the mug to affect the sensor, while also simulating the time it would take a prosthesis user to drink from the vessel. The 60 s wait reduces the effects of drift (as seen in Fig. 2(d)) by allowing the sensor to return to its original size before the next grasp. In the grasping phase of every cycle, a linear jump in resistance can be observed. This is then followed by a relaxation period during the hold phase, which could be attributed to the poor adhesion and sliding of the sensor on the robotic hand or mechanical properties of the elastomer substrate, then a smaller jump in resistance arises as the hand opens. The divergence of the hot and cold curves in Fig. 4(d) can be attributed to sensor sliding prior to the cold grasps, and the colder temperature slowing down the contraction of the elastomer substrate between grasps, causing increased drift overall. It is important to note, however, that this does not necessarily reflect the strain responses of the sensor when actively heated or cooled. Although it was impossible to precisely control the amount of strain applied to the sensor through manual operation, the changes in resistance during the grasping phases, when the sensor is being actively heated or cooled, are minor. Fig. 4(e) demonstrates the similarity in strain sensing behavior between the hot and cold grasps during each grasping phase, showing that the sensor output is identical regardless of the environmental temperature. For clarity, the active grasping curves, highlighted in Fig. 4(d), have been isolated and overlaid in Fig. 4(e) by shifting the peaks to coincide, while preserving the original measurement ranges. We quantified the influence of temperature as the percentage resistance change between the peak of each grasp and the value recorded after 37 s of holding the mug. This allows time for the temperature of the mug to affect the sensor and potentially influence the behavior of the LIG–PDMS nanocomposite and leaves buffer time to minimize human error. The thermal influence values are 11.1%, 8.5% and 7.1%, respectively, for the hot mug and 11.1%, 8.9% and 8.1%, respectively, for the cold mug. Thermally induced noise in this case is the average difference between the drop of resistance of the hot mug, and that of the cold mug over all 3 grasps, making it approximately 0.5% overall. The SNR is calculated to be around 29 by dividing the average peak resistance change of all grasps (14.3%) by the average thermally induced noise value (0.5%). For comparison, this experiment was repeated with a 20_13 sensor, which showed consistent thermally induced deviations in resistance during grasping and an SNR of 11 (Fig. S11). This experiment proves that, even in a practical scenario, the influence of reducing the temperature

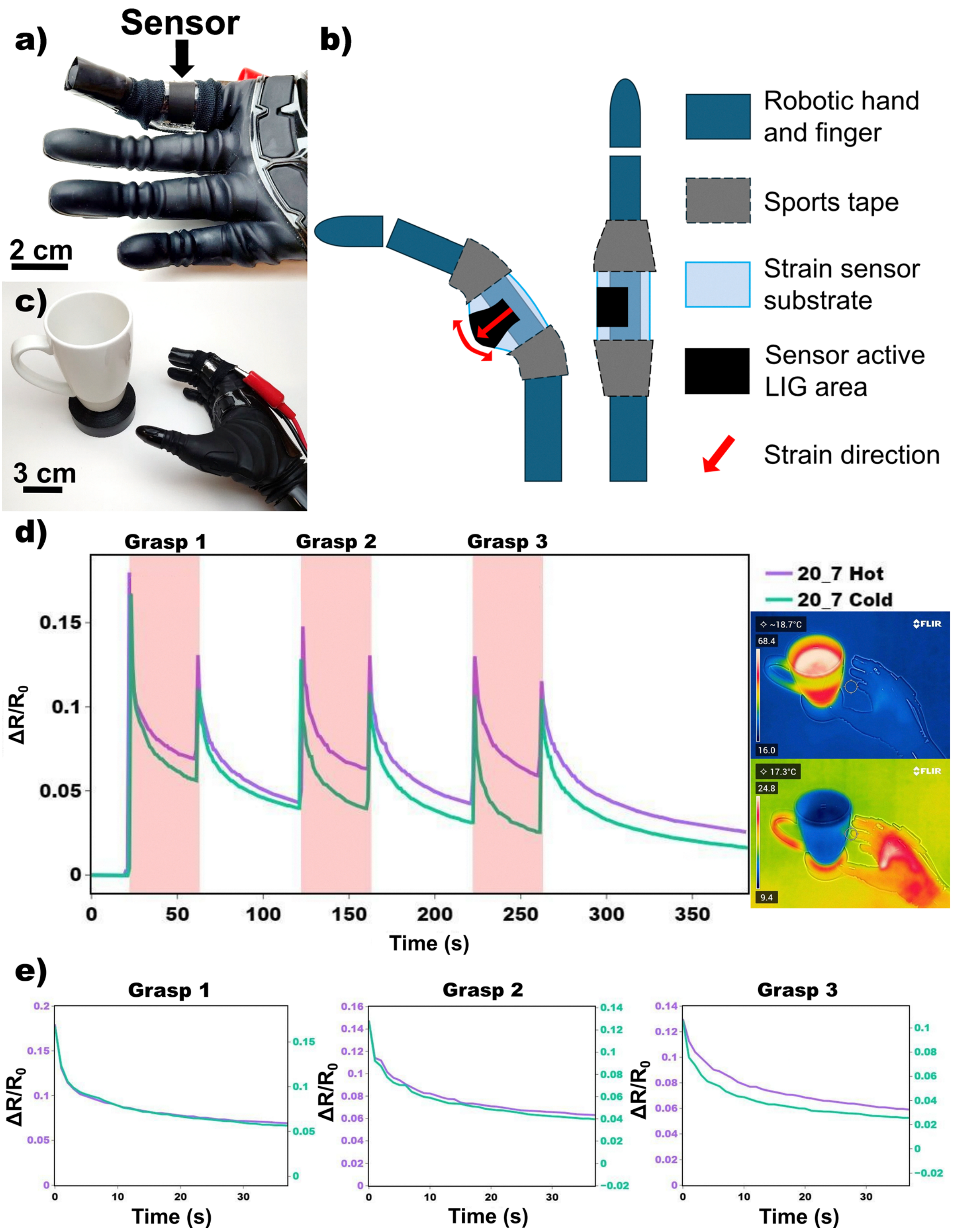

Fig. 4 (a) Photograph of a 20_7 sensor wrapped around the finger of a Covvi™ robotic prosthetic hand and secured with kinesiology tape to sense strain when the finger is bent during grasping. (b) A schematic showing how strain is induced in the sensor *via* finger bending and bulging of the nanocomposite. (c) Application scenario of grasping a mug when it is hot or cold. (d) Strain response of the sensor while grasping the mug when it is filled with hot (∼70 °C) and cold (∼8 °C) water, including thermal images of the scenario. (e) Sensor signals from each grasping phase, overlaid to demonstrate contact heating effects without the influence of sensor drift.

sensitivity of the LIG–PDMS sensors by altering the induction laser parameters is significant. Applying this practice to the creation of LIG–polymer nanocomposite soft sensors and e-skins in the future could make robotic prostheses easier for users to control while receiving accurate sensory feedback in any environment.

Soft electrothermal actuators with integrated sensing function

In another example, we developed electrothermal actuators inspired by the work of Wang *et al.*[81,82] The fundamental idea behind this design was to exploit the inherent thermal stability of LIG–PDMS nanocomposite sensors, enabling them to maintain consistent resistance even under actuation at elevated temperatures, up to 100 °C. The fabrication process of the LIG-based soft actuators, as illustrated in Fig. S12, began with laser scribing of LIG patterns onto a PI film. This was achieved using optimized laser parameters of 20% power and 7% speed. A layer of PDMS solution was then spin-coated onto the LIG. Following the curing and peeling off processes, the structure was cut based on predetermined U-shaped designs and a layer of commercial PI tape was applied on top of the PDMS, forming a bilayer structure with the nanocomposite sensing layer sandwiched between PDMS and PI layers. Upon applying a voltage, the LIG nanocomposite experiences heating due to the Joule effect, reaching temperatures up to 100 °C. Notably, PDMS exhibits a significantly higher CTE compared to the relatively low CTE of PI ($\sim 40 \times 10^{-6}$ $°C^{-1}$).[81] This substantial difference leads to asymmetric thermal expansion, causing deformation in the actuator. This asymmetric response is demonstrated in Fig. 5(a) and Movie S2, which illustrates the bending movement of the actuator towards the PI layer as a result of differential thermal expansion. Fig. 5(b) demonstrates the resistance response of a soft actuator under free bending and when fully blocked. The LIG film showed a 23.5% relative change in resistance during free bending while a 1.3% change was observed when the actuator was constrained, preventing bending strain in the sensing film. In both cases, the measured temperature difference between the blocked and unblocked states was less than 5%. This shows an 18-fold greater response in the free-bending condition, confirming that the alteration in resistance observed in the sensor during actuation arises exclusively from mechanical deformation, rather than an increase in temperature. Fig. 5(c) illustrates additional experiments on the sensing capability of the soft actuator. An actuator was subjected to a controlled voltage for bending actuation while it was moved across a custom 3D-printed track. As shown in Fig. 5(d) and Movie S3, the actuator can detect its level of deflection by monitoring changes in the nanocomposite's electrical resistance. When the actuator shifts upon contact with the surface, its resistance changes accordingly. This self-sensing capability enables visualization of the shapes encountered by the soft actuator without additional sensors.

3 Conclusion

In summary, this paper introduced a widely accessible approach to enhance the functionality of LIG–PDMS nanocomposites by adjusting the laser induction process to minimize thermal sensitivity. The manipulation of laser parameters enabled control over the carbonization process, leading to the

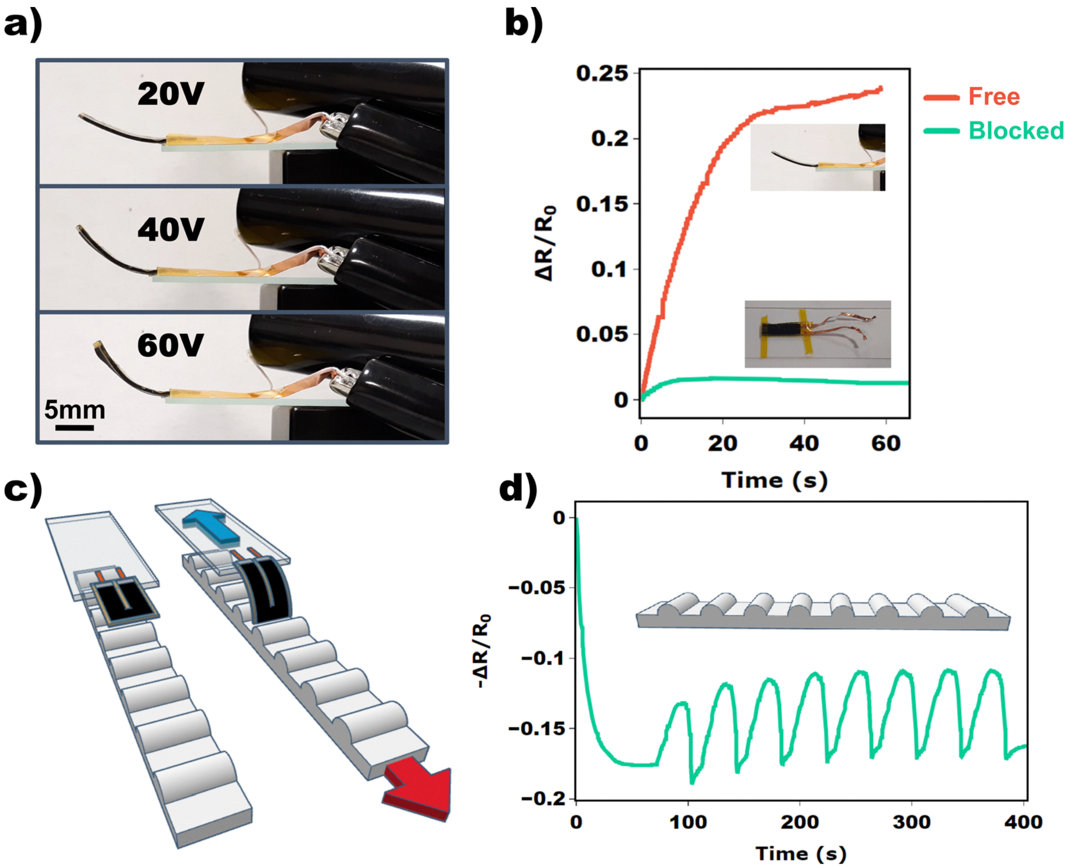

Fig. 5 (a) Deformation of a soft electrothermal actuator at different voltages. (b) Relative resistance changes of a soft actuator subjected to 20 V under free bending and when fully blocked. (c) Schematics of a soft actuator sliding over a 3D-printed terrain. (d) Sensing response of the actuator during the sliding movement.

formation of varied microstructure networks within the nanocomposites. These microstructural variations resulted in diminished sensitivities to temperature, allowing for the design and fabrication of soft strain sensors with significantly diminished TCRs and self-sensing electrothermal soft actuators with negligible temperature sensitivities. Finally, the potential applications of the optimized strain sensors were demonstrated in an environment with significant temperature fluctuations, and the wider versatility of the laser-tuned LIG nanocomposites was demonstrated by self-sensing thermal actuators.

Beyond biomedical and soft robotic applications, the thermal stability of these nanocomposites opens possibilities for their use in harsh or dynamic environments, such as aerospace systems, structural health monitoring of buildings or bridges, and smart textiles for adaptive clothing. Future research could focus on enhancing the durability and sensitivity of the sensors for prolonged use, as well as scaling up their production for commercial applications. Additionally, exploring their integration with wireless or AI-driven systems could further broaden their impact in fields such as autonomous healthcare, disaster response robotics, and environmental monitoring.

4 Experimental section

Fabrication of LIG–PDMS nanocomposite sensors

PI films with a thickness of 150 μm (Craftbot adhesive Kapton sheet) were used as the starting material for graphene production. A commercial CO_2 laser cutter (Trotec™ Speedy 100, max. laser power 60 W, max. processing speed 2.8 m s^{-1} at 1000 points per inch pulse rate) was employed to convert the PI films into LIG using various power and speed settings in a standard area of 10×30 mm^2 per sample. To fabricate the LIG–PDMS nanocomposite sensors, a 10 : 1 mixture of PDMS base and curing agent (SYLGARD™ 184 from Dow) was prepared. The mixture was thoroughly degassed at 0.3 bar for 10 minutes and then poured onto the carbonized film to achieve a uniform coating in an area of 16×40 mm^2 at a uniform thickness of approximately 1.5 mm. Subsequently, the samples were degassed for a further 10 minutes and cured at 100 °C for one hour. PDMS films with embedded LIG nanocomposite layers were peeled off from PI films. Aluminum foil electrodes were attached to each side of the nanocomposite films using silver epoxy (MG Chemicals 9410, one-part epoxy) and cured at 150 °C for 10 minutes. For the raw samples, the silver epoxy was applied directly onto the graphene without the addition of PDMS.

Electrical, electromechanical, and electrothermomechanical characterizations

We investigated the *I–V* characteristics of both pure LIG and LIG–PDMS nanocomposite. For each sample, the voltage was swept in steps of 0.5 V over a range of −10 V to +10 V (Tenma 72-2535), and the corresponding current was recorded (Keysight U1241C). The measurements were performed at room temperature under ambient conditions. For the electromechanical measurements, the LIG–PDMS nanocomposite sensors were mounted and secured on a motorized moving stage (Zaber X-LRQ450HP-DE51) using a custom 3D-printed jig. Both ends of the sensors were connected to a data acquisition board (NI USB6363, National Instruments) to measure the voltage across the sensors. A reference resistor with a known resistance was employed to precisely measure the electrical resistance of sensors under various mechanical loading conditions. A custom-made LabVIEW script was used to control the movement of the moving stage and record the displacement, resistance, and time during the dynamic electromechanical measurements. For dynamic electrothermomechanical testing, a soldering station (858D SMD Hot Air Rework Soldering Station) was placed at a distance of 2 cm from each sensor and set at a temperature of 100 °C to heat the samples while a FLIR IR thermal camera (E5-XT Wi-Fi Thermal Imaging Camera) was utilized to measure their surface temperature (see Fig. S13). For the static electrothermal testing, the nanocomposite sensors were placed on a Creality Ender 3 Pro 3D printer heated bed and connected to the data acquisition board. A custom Python script was developed to control the heating profile of the printer bed. The resistance values of each sensor were recorded using the custom LabVIEW script. In addition, an auxiliary loop incorporated a DC95F103WN negative temperature coefficient thermistor (Amphenol Advanced Sensors), placed in close proximity to sensors, and a second reference resistor to monitor the temperature experienced by sensors (see Fig. S14). The observed plateau in Fig. 2(a) measurements near 60 °C arises from limitations in the experimental setup. Specifically, the thermistor was not positioned identically to the samples, and the temperature distribution across the 3D-printer heated bed was not entirely uniform. These factors introduced increased discrepancies at higher temperatures, which manifested as the apparent plateau in measurements.

Materials characterizations

Raman spectroscopy was performed to analyze the structural properties of the LIG produced from PI films. The Raman spectra were acquired using a confocal Raman microscope (LabRAM HR, Horiba Jobin Yvon) equipped with a laser source at a wavelength of 532 nm (Ventus 532 laser system, 100 mW). Prior to the measurements, the LIG samples were placed on a microscope slide and positioned under the Raman microscope. The Raman spectra were collected in the range of 1000–3000 cm^{-1} with an integration time of 10–20 s per spectrum. The acquired Raman spectra were analyzed to determine characteristic features such as the G, D, and 2D bands. The intensity ratio of the D and G bands (I_G/I_D) was calculated to assess the quality and structural characteristics of the LIG.[76,83] The interpretation of these Raman bands provides valuable information about the degree of graphitization, presence of defects, and structural integrity of the LIG samples. The intensity ratio I_G/I_D serves as a measure of the graphene crystallinity and defect density.[74,76] SEM (Tescan Clara) was employed to study the microstructure of the pristine LIG and nanocomposite films.

Strain sensor applications

For prosthetic application, a 20_7 sensor with a dimension of 25 × 75 mm^2 was utilized. Thin strips of aluminum foil (10 × 5 mm^2) were applied with silver epoxy to secure wires to each end of the sensor. All measurements were recorded by a Keysight U1241C digital multimeter and logged by the Keysight Logger software. For the soft actuator application, LIG patterns (15 × 5 mm^2) were scribed onto a PI film using optimized laser parameters of 20% power and 7% speed. Following the LIG formation, a layer of PDMS solution was spin-coated onto the LIG surface at 500 rpm for 5 seconds to ensure uniform coverage. The coated samples were then cured at 90 °C for one hour to allow complete polymerization of the PDMS. Once cured, the LIG–PDMS nanocomposite was carefully peeled off from the substrate. Subsequently, electrodes were affixed to the ends of the LIG track using silver epoxy to facilitate electrical contact. After electrode placement, the nanocomposite was trimmed according to predetermined geometric designs. To complete the fabrication of the soft actuator, a layer of commercial PI tape was applied to the top surface of the PDMS, resulting in a bilayer soft actuator. Actuation of the LIG-based sensor was achieved using a DC power supply, where the applied output voltage controlled the deformation of the actuator. Current measurements were recorded using a Keysight U1242C digital multimeter wired in series with the sensor and data were collected through the Keysight Logger Software.

Author contributions

TJ: conceptualization, methodology, investigation, software, visualization, writing – original draft, writing – review & editing, formal analysis. SW: conceptualization, methodology, investigation, software, visualization, writing – original draft, writing – review & editing. IP: writing – review & editing. AAS: writing – review & editing, supervision. HH: supervision, writing – review & editing. TL: writing – review & editing, supervision. MA: project administration, funding acquisition, resources, supervision, writing – review & editing.

Conflicts of interest

There are no conflicts to declare.

Data availability

All data gathered for this work have been uploaded to the materials data facility repository, available *via* this link: **https://doi.org/10.18126/e1f9-bn46**.

Supplementary information is available. See DOI: **https://doi.org/10.1039/d5tc02865e**.

Acknowledgements

This work was partially funded by the Engineering and Physical Sciences Research Council (EPSRC) [grant number EP/S023208/1], part of United Kingdom Research and Innovation (UKRI). The authors thank Touchlab Ltd. for offering a laser engraver to manufacture LIG nanocomposite strain sensors. The authors thank Alistair McConnell at Heriot-Watt University for providing the Covvi™ prosthetic hand for the application experiment, and Dr Venkatarao Selamneni from University of Glasgow for taking cross-sectional SEM images. The AI tool "ChatGPT" was used in a closely supervised manner to improve text formatting and grammar.

References

1 D. V. Dimitrov, *Healthc. Inform. Res.*, 2016, **22**, 156–163.
2 R. Pastorino, C. De Vito, G. Migliara, K. Glocker, I. Binenbaum, W. Ricciardi and S. Boccia, *Eur J Public Health*, 2019, **29**, 23–27.
3 M. Lin, H. Hu, S. Zhou and S. Xu, *Nat. Rev. Mater.*, 2022, **7**, 850–869.
4 J. Li, H. Jia, J. Zhou, X. Huang, L. Xu, S. Jia, Z. Gao, K. Yao, D. Li, B. Zhang, Y. Liu, Y. Huang, Y. Hu, G. Zhao, Z. Xu, J. Li, C. K. Yiu, Y. Gao, M. Wu, Y. Jiao, Q. Zhang, X. Tai, R. H. Chan, Y. Zhang, X. Ma and X. Yu, *Nat. Commun.*, 2023, **14**, 5009.
5 X. Cheng, J. Cai, J. Xu and D. Gong, *ACS Appl. Mater. Interfaces*, 2022, **14**, 39230–39239.
6 S. Xu, D. M. Vogt, W. H. Hsu, J. Osborne, T. Walsh, J. R. Foster, S. K. Sullivan, V. C. Smith, A. Rousing, E. C. Goldfield and R. J. Wood, *Adv. Funct. Mater.*, 2019, **29**, 1970038.
7 X. Wang, Y. Tao, S. Pan, X. Fang, C. Lou, Y. Xu, J. Wu, M. Sang, L. Lu, X. Gong, T. Luo and S. Xuan, *npj Flexible Electron.*, 2022, **6**, 95.
8 Y. Wang, Z. Xie, H. Huang and X. Liang, *Smart Med.*, 2024, **3**, e20230045.
9 P. Capsi-Morales, C. Piazza, M. G. Catalano, G. Grioli, L. Schiavon, E. Fiaschi and A. Bicchi, *Sci. Rep.*, 2021, **11**, 23952.
10 S. R. Kim, J. H. Kim and J. W. Park, *ACS Appl. Mater. Interfaces*, 2017, **9**, 26407–26416.
11 M. Amjadi, A. Pichitpajongkit, S. Lee, S. Ryu and I. Park, *ACS Nano*, 2014, **8**, 5154–5163.
12 J. Choi, J. Min, D. Kim, J. Kim, J. Kim, H. Yoon, J. Lee, Y. Jeong, C. Y. Kim and S. H. Ko, *ACS Nano*, 2023, **17**, 17966–17978.
13 K. K. Kim, S. Hong, H. M. Cho, J. Lee, Y. D. Suh, J. Ham and S. H. Ko, *Nano Lett.*, 2015, **15**, 5240–5247.
14 H. Yoon, J. Choi, J. Kim, J. Kim, J. Min, D. Kim, S. Jeong, J. G. Lee, J. Bang, S. H. Choi, Y. Jeong, C. Y. Kim and S. H. Ko, *Adv. Funct. Mater.*, 2024, **34**, 2313504.
15 K. K. Kim, M. Kim, K. Pyun, J. Kim, J. Min, S. Koh, S. E. Root, J. Kim, B.-N. T. Nguyen, Y. Nishio, S. Han, J. Choi, C.-Y. Kim, J. B.-H. Tok, S. Jo, S. H. Ko and Z. Bao, *Nat. Electron.*, 2023, **6**, 64–75.
16 J. J. Park, S. Hong, Y. Jung, P. Won, C. Majidi, M. Kim and S. H. Ko, *Adv. Funct. Mater.*, 2025, 2505089.
17 I. Kang, M. J. Schulz, J. H. Kim, V. Shanov and D. Shi, *Smart Mater. Struct.*, 2006, **15**, 737–748.

18 Q. Liu, S. Zhao, T. Hu, C. Jiang and B. Sheng, *IEEE Sens. J.*, 2023, **23**, 8268–8276.

19 S. Sharma, G. B. Pradhan, S. Jeong, S. Zhang, H. Song and J. Y. Park, *ACS Nano*, 2023, **17**, 8355–8366.

20 H. Liu, Q. Li, S. Zhang, R. Yin, X. Liu, Y. He, K. Dai, C. Shan, J. Guo, C. Liu, C. Shen, X. Wang, N. Wang, Z. Wang, R. Wei and Z. Guo, *J. Mater. Chem. C*, 2018, **6**, 12121–12141.

21 Z. Shen, Z. Zhang, N. Zhang, J. Li, P. Zhou, F. Hu, Y. Rong, B. Lu and G. Gu, *Adv. Mater.*, 2022, **34**, e2203650.

22 M. Amjadi, K. U. Kyung, I. Park and M. Sitti, *Adv. Funct. Mater.*, 2016, **26**, 1678–1698.

23 Z. Yao, H. Feng, K. Shang, X. Deng and T. Yang, *ACS Appl. Nano Mater.*, 2023, **6**, 6550–6558.

24 X. Shi, L. Zhu, H. Yu, Z. Tang, S. Lu, H. Yin, M. You, G. Sun and Q. Chen, *Adv. Funct. Mater.*, 2023, **33**, 2301036.

25 S. Wu, K. Moody, A. Kollipara and Y. Zhu, *ACS Appl. Mater. Interfaces*, 2023, **15**, 1798–1807.

26 D. Kang, P. V. Pikhitsa, Y. W. Choi, C. Lee, S. S. Shin, L. Piao, B. Park, K. Y. Suh, T. I. Kim and M. Choi, *Nature*, 2014, **516**, 222–226.

27 G. F. Hawes, P. Verma, M. Uceda, G. Karimi, B. S. Noremberg and M. A. Pope, *ACS Appl. Mater. Interfaces*, 2023, **15**, 10570–10584.

28 Q. Zhang, F. Zhang, X. Liu, Z. Yue, X. Chen and Z. Wan, *Adv. Mater. Technol.*, 2023, **8**, 2300244.

29 D. Kim, A. Chhetry, M. A. Zahed, S. Sharma, S. Jeong, H. Song and J. Y. Park, *ACS Appl. Mater. Interfaces*, 2023, **15**, 1475–1485.

30 J. Li, Z. Yao, X. Meng, X. Zhang, Z. Wang, J. Wang, G. Ma, L. Liu, J. Zhang, S. Niu, Z. Han and L. Ren, *ACS Nano*, 2024, **18**, 2520–2530.

31 Y. Wu, H. Tang, L. Wang, Y. Zong, J. Jia, L. Sun and K. Niu, *Compos. Sci. Technol.*, 2023, **242**, 110190.

32 M. Amjadi, Y. J. Yoon and I. Park, *Nanotechnology*, 2015, **26**, 375501.

33 M. Amjadi and M. Sitti, *Adv. Sci.*, 2018, **5**, 1800239.

34 Y. Jung, K. R. Pyun, S. Yu, J. Ahn, J. Kim, J. J. Park, M. J. Lee, B. Lee, D. Won, J. Bang and S. H. Ko, *Nano-Micro Lett.*, 2025, **17**, 127.

35 D. Won, H. Kim, J. Kim, H. Kim, M. W. Kim, J. Ahn, K. Min, Y. Lee, S. Hong, J. Choi, C. Y. Kim, T.-S. Kim and S. H. Ko, *Nat. Electron.*, 2024, **7**, 475–486.

36 D. Won, J. Kim, J. Choi, H. Kim, S. Han, I. Ha, J. Bang, K. K. Kim, Y. Lee, T. S. Kim, J. H. Park, C. Y. Kim and S. H. Ko, *Sci. Adv.*, 2022, **8**, eabo3209.

37 I. Hong, S. Lee, D. Kim, H. Cho, Y. Roh, H. An, S. Hong, S. H. Ko and S. Han, *Nanotechnology*, 2019, **30**, 074001.

38 J. Lin, Z. Peng, Y. Liu, F. Ruiz-Zepeda, R. Ye, E. L. Samuel, M. J. Yacaman, B. I. Yakobson and J. M. Tour, *Nat. Commun.*, 2014, **5**, 5714.

39 T. S. D. Le, H. P. Phan, S. Kwon, S. Park, Y. Jung, J. Min, B. J. Chun, H. Yoon, S. H. Ko, S. W. Kim and Y. J. Kim, *Adv. Funct. Mater.*, 2022, **32**, 2270276.

40 E. E. Ortelli, F. Geiger, T. Lippert, J. Wei and A. Wokaun, *Macromolecules*, 2000, **33**, 5090–5097.

41 N.-K. Yang, Y.-K. Shin, S. Park, S.-M. Kim, B.-J. Koo, J. Jeong and M.-H. Seo, *Micro Nano Syst. Lett.*, 2024, **12**, 8.

42 K. Avinash and F. Patolsky, *Mater. Today*, 2023, **70**, 104–136.

43 Y. Guo, C. Zhang, Y. Chen and Z. Nie, *Nanomaterials*, 2022, **12**, 2336.

44 R. Ye, D. K. James and J. M. Tour, *Adv. Mater.*, 2019, **31**, e1803621.

45 Z. Zhang, H. Zhu, W. Zhang, Z. Zhang, J. Lu, K. Xu, Y. Liu and V. Saetang, *Carbon*, 2023, **214**, 118356.

46 W. Liu, Y. Huang, Y. Peng, M. Walczak, D. Wang, Q. Chen, Z. Liu and L. Li, *ACS Appl. Nano Mater.*, 2020, **3**, 283–293.

47 H. Yu, J. Bian, F. Chen, J. Ji and Y. Huang, *Adv. Electron. Mater.*, 2022, **9**, 2201086.

48 Y. H. Yen, C. S. Hsu, Z. Y. Lei, H. J. Wang, C. Y. Su, C. L. Dai and Y. C. Tsai, *Micromachines*, 2022, **13**, 1220.

49 H. Tian, Y. Shu, X. F. Wang, M. A. Mohammad, Z. Bie, Q. Y. Xie, C. Li, W. T. Mi, Y. Yang and T. L. Ren, *Sci. Rep.*, 2015, **5**, 8603.

50 L. Huang, H. Wang, D. Zhan and F. Fang, *IEEE Sens. J.*, 2021, **21**, 12048–12056.

51 M. G. Stanford, K. Yang, Y. Chyan, C. Kittrell and J. M. Tour, *ACS Nano*, 2019, **13**, 3474–3482.

52 Z. Wan, N.-T. Nguyen, Y. Gao and Q. Li, *Sustainable Mater. Technol.*, 2020, **25**, e00205.

53 F. M. Vivaldi, A. Dallinger, A. Bonini, N. Poma, L. Sembranti, D. Biagini, P. Salvo, F. Greco and F. Di Francesco, *ACS Appl. Mater. Interfaces*, 2021, **13**, 30245–30260.

54 Y. Houeix, D. Gerardo, S. Gómez-Gijón, V. Toral, N. Rodríguez, D. P. Morales and A. Rivadeneyra, *Adv. Sustain. Syst.*, 2024, **8**, 2300606.

55 H. K. Nam, T. S. D. Le, D. Yang, B. Kim, Y. Lee, J. S. Hwang, Y. R. Kim, H. Yoon, S. W. Kim and Y. J. Kim, *Adv. Mater. Technol.*, 2023, **8**, 2201952.

56 X. Li, D. Su, Y. Gu, J. Zhang, S. Li, Y. Xiao, J. He, W. Wang and D. Li, *Appl. Mater. Today*, 2024, **36**, 102051.

57 S. Zhu, Z. Lei, Y. Dou, C.-W. Lou, J.-H. Lin and J. Li, *Chem. Eng. J.*, 2023, **452**, 139403.

58 R. Ye, Y. Chyan, J. Zhang, Y. Li, X. Han, C. Kittrell and J. M. Tour, *Adv. Mater.*, 2017, **29**, 1702211.

59 Y. Jung, J. Min, J. Choi, J. Bang, S. Jeong, K. R. Pyun, J. Ahn, Y. Cho, S. Hong, S. Hong, J. Lee and S. H. Ko, *Appl. Mater. Today*, 2022, **29**, 101589.

60 J. Min, Y. Jung, J. Ahn, J. G. Lee, J. Lee and S. H. Ko, *Adv. Mater.*, 2023, **35**, e2211273.

61 H. Yang, Q. Huang, S. Wang, Q. Zong, C. Tan, H. Ye and G. Zhang, *Appl. Surf. Sci.*, 2024, **660**, 159885.

62 Y. Yue, X. Li, Z. Zhao, H. Wang and X. Guo, *Soft Sci.*, 2023, **3**, 13.

63 F. Liu, Y. Gao, G. Wang, D. Wang, Y. Wang, M. He, X. Ding, H. Duan and S. Luo, *Adv. Sci.*, 2023, **10**, e2204990.

64 B. Kulyk, B. F. R. Silva, A. F. Carvalho, P. Barbosa, A. V. Girão, J. Deuermeier, A. J. S. Fernandes, F. M. L. Figueiredo, E. Fortunato and F. M. Costa, *Adv. Mater. Technol.*, 2022, **7**, 2101311.

65 L. Huang, H. Wang, P. Wu, W. Huang, W. Gao, F. Fang, N. Cai, R. Chen and Z. Zhu, *Sensors*, 2020, **20**, 4266.

66 W. Wang, L. Lu, Z. Li, L. Lin, Z. Liang, X. Lu and Y. Xie, *ACS Appl. Mater. Interfaces*, 2022, **14**, 1315–1325.

67 H. Wang, Z. Xiang, P. Zhao, J. Wan, L. Miao, H. Guo, C. Xu, W. Zhao, M. Han and H. Zhang, *ACS Nano*, 2022, **16**, 14679–14692.

68 V. Fiodorov, R. Trusovas, Z. Mockus, K. Ratautas and G. Raciukaitis, *Polymers*, 2023, **15**, 4229.

69 L. Wang, Z. Wang, A. N. Bakhtiyari and H. Zheng, *Micromachines*, 2020, **11**, 1094.

70 A. Nag, R. B. V. B. Simorangkir, D. R. Gawade, S. Nuthalapati, J. L. Buckley, B. O'Flynn, M. E. Altinsoy and S. C. Mukhopadhyay, *Mater. Des.*, 2022, **221**, 110971.

71 S. J. Clarson and J. A. Semlyen, *Siloxane Polymers*, Prentice Hall, 1993.

72 C. Zhang, J. Sun, Y. Lu and J. Liu, *J. Mater. Chem. C*, 2021, **9**, 754–772.

73 S. Han, X. Zhang, P. Wang, J. Dai, G. Guo, Q. Meng and J. Ma, *Polym. Test.*, 2021, **98**, 107178.

74 A. C. Ferrari and D. M. Basko, *Nat. Nanotechnol.*, 2013, **8**, 235–246.

75 L. M. Malard, M. A. Pimenta, G. Dresselhaus and M. S. Dresselhaus, *Phys. Rep.*, 2009, **473**, 51–87.

76 C. Cong, T. Yu, K. Sato, J. Shang, R. Saito, G. F. Dresselhaus and M. S. Dresselhaus, *ACS Nano*, 2011, **5**, 8760–8768.

77 W.-B. Zhu, S.-S. Xue, H. Zhang, Y.-Y. Wang, P. Huang, Z.-H. Tang, Y.-Q. Li and S.-Y. Fu, *J. Mater. Chem. C*, 2022, **10**, 8226–8233.

78 S. Niu, X. Chang, Z. Zhu, Z. Qin, J. Li, Y. Jiang, D. Wang, C. Yang, Y. Gao and S. Sun, *ACS Appl. Mater. Interfaces*, 2021, **13**, 55307–55318.

79 N. Thomas, A. J. Miller, H. Ayaz and J. D. Brown, *Sci. Rep.*, 2023, **13**, 484.

80 G. Gu, N. Zhang, H. Xu, S. Lin, Y. Yu, G. Chai, L. Ge, H. Yang, Q. Shao, X. Sheng, X. Zhu and X. Zhao, *Nat. Biomed. Eng.*, 2021, **7**, 589–598.

81 H. Wang, Z. Zhao, P. Liu, Y. Pan and X. Guo, *ACS Appl. Mater. Interfaces*, 2022, **14**, 41283–41295.

82 H. Wang, X. Li, X. Wang, Y. Qin, Y. Pan and X. Guo, *Small*, 2024, **20**, e2310612.

83 L. G. Cancado, A. Jorio, E. H. Ferreira, F. Stavale, C. A. Achete, R. B. Capaz, M. V. Moutinho, A. Lombardo, T. S. Kulmala and A. C. Ferrari, *Nano Lett.*, 2011, **11**, 3190–3196.